

Highlighting research from the labs of Prof. Sophie Hermans and Prof. Yaroslav Filinchuk at the Institute of Condensed Matter and Nanosciences, Catholic University of Louvain, Belgium.

Green synthesis of a large series of bimetallic MIL-100(Fe,M) MOFs

A large variety of MIL-100(Fe,M), metal-doped iron-based MOFs with high thermal stability and surface areas, were obtained through a new scalable and green methodology. This water-based synthesis can be applied to doping with p-, d- and f-elements in oxidation states from +I to +V, therefore being widely applicable.

As featured in:



See Timothy Steenhaut, Sophie Hermans, Yaroslav Filinchuk, *New J. Chem.*, 2020, **44**, 3847.

PAPER



Cite this: *New J. Chem.*, 2020,
44, 3847

Received 15th January 2020,
Accepted 3rd February 2020

DOI: 10.1039/d0nj00257g

rsc.li/njc

Green synthesis of a large series of bimetallic MIL-100(Fe,M) MOFs†

Timothy Steenhaut,^{ib}* Sophie Hermans^{ib}* and Yaroslav Filinchuk^{ib}*

Here we present a scalable and green methodology to synthesize a large variety of MIL-100(Fe,M), metal-doped iron-based MOFs with high thermal stability and surface areas. Our synthesis is performed at room temperature in aqueous media and can be applied to doping with p-, d- and f-elements in oxidation states from +I to +V, therefore being highly general. The influence of the doping metal nature on the thermal and textural properties is systematically investigated. We show that large differences between the ionic radius of the doping and the templating metals does not lead to phase segregation. The incorporation of Cu(I) drastically lowers the thermal stability of MIL-100(Fe,Cu), while the incorporation of V, Al and Ti induces the formation of mesopores. Finally, we developed a PXRD-based method that can be combined with TGA to easily access the metal ratios in complex mixed-metal MOFs.

Introduction

Porous materials are essential in several fields such as gas sorption,^{1,2} catalysis,^{3–5} chemical separation,⁶ sensing,^{7,8} heat transformation,⁹ *etc.* Metal-organic frameworks (MOFs) in particular, being porous coordination compounds made of metallic clusters and organic bridging ligands, are one of the most recent developments in this field. However, for many years their applications were limited due to their low stability and difficulty to synthesize at low cost and on a large scale.^{10,11} Recent work allowed obtaining several types of stable MOFs that can withstand high temperatures and large panels of solvents.^{12,13} However, the synthesis of such compounds still largely suffers from inconvenient preparation procedures,¹⁴ although some progress has recently been made towards greener synthetic procedures.^{15–17} The most stable MOFs are usually obtained from combinations of ligands and metals with a high affinity, which are most of the time assembled by solvothermal processes to avoid precipitation of amorphous compounds. Those procedures are energy and time consuming and improvement in the synthetic approaches is thus necessary to render MOFs of industrial importance.¹⁸

Among remarkably stable MOFs, MIL-100 derivatives show quite interesting properties (see Table 1),¹⁹ like high surface areas up to more than 2000 m² g⁻¹, thermal stability and resistance to solvents.²⁰ Their structures are composed of

[M₃O(X)(H₂O)₂]⁶⁺ clusters (M = Fe, Al, Cr, Sc, In, V or mixed metal, see M₁ and M₂ in Table 1; X = OH⁻, Cl⁻, F⁻) linked by benzenetricarboxylate (BTC³⁻) ligands.

Iron centers in MIL-100(Fe) have been shown active in catalysis and gas sorption.^{21–23} It was shown that adding a doping metal into the structure can impressively improve some properties of MOFs and MIL-100 in particular.^{24–27} However, until now, very few combinations of template and doping metals were investigated and all those materials were synthesized by solvothermal methods that mostly involve the use of dangerous acids like HNO₃ or HF as modulators. In some cases, the second metal was introduced by post-synthetic exchange, adding a second step in the synthesis. Moreover, the possibility of mixing metals with large differences of ionic radii in the MIL-100 structure has not been investigated yet.

Our goal is to introduce a wide range of metal substitutions into the Fe-based MIL-100, serving as a low-cost templating structure; iron having the advantages of being very abundant, cheap and non-toxic. We started with an improvement of the synthesis of pure MIL-100(Fe). Apart from solvothermal procedures (Table 1), it can also be obtained in mild conditions by mixing solutions of iron(II) chloride and trimesic acid (H₃BTC) deprotonated with NaOH in a basic environment.^{28,29} We quickly found that this procedure is reproducible and scalable but does not allow incorporating any doping metal by simply adding a second salt along with FeCl₂. Inspired by an earlier work on other MOFs,³⁰ we modified the reported procedure by using the sodium salt of trimesic acid, Na₃BTC·3H₂O, in slightly acidic environment. We also used iron(II) sulphate as iron source instead of the corresponding chloride because of its lower cost and better suitability for industrial needs as it does not present

Université Catholique de Louvain, MOST, Place Louis Pasteur 1,
1348 Louvain-la-Neuve, Belgium. E-mail: timothy.steenhaut@uclouvain.be,
sophie.hermans@uclouvain.be, Yaroslav.Filinchuk@uclouvain.be

† Electronic supplementary information (ESI) available. See DOI: 10.1039/d0nj00257g

Table 1 Mono- and bimetallic MIL-100(M₁,M₂) MOFs described in the literature to this date, their synthesis methods and applications

M1	M2	Synthesis method	Application	Ref.
Cr, V or Sc	—	Solvothermal	CO ₂ adsorption	33
Sc	Al, Cr or Fe	Hydrothermal and solvothermal	Friedel–Crafts, oxidation and tandem catalysis	34
Al, Cr, Sc or V	—	Solvothermal	Catalytic tetrahydropyranlation	35
V, Al, Fe or Cr	—	Solvothermal	Catalytic condensation of glycerol with acetone	36
Al, Cr, Fe, In, Sc or V	—	Solvothermal	Prins condensation of β-pinene and formaldehyde	37
Fe	Mn	Hydrothermal (with HF)	Catalytic reduction of NO _x by NH ₃	38
Sc	Ti	Solvothermal, post-synthetic exchange; high valence metal metathesis and oxidation	Photodegradation of methylene blue	39
Ti	—	Solvothermal	Photocatalysis	40
Fe	Ni	Hydrothermal, HNO ₃ assisted	Prins reaction of β-pinene and paraformaldehyde	41

the corrosion issues occurring in the presence of chloride ions.³¹ This allowed us to incorporate many metals in +II, +III and +IV oxidation states into the structure in a green single-step synthesis.

We also demonstrate that we can control the amount of doping metal in the structure and that metals with large ionic radii (Fig. 1),³² such as lanthanides, can also be incorporated into the MIL-100(Fe) structure. Finally, we present a new convenient way to determine the percentage of a doping metal in MOFs by powder X-ray diffraction (PXRD).

Results and discussion

New green synthesis of MIL-100(Fe) and incorporation of Co

The synthesis of MIL-100(Fe) in aqueous media at room temperature is possible both in slightly acidic and in slightly basic conditions. While the reaction products are both MIL-100(Fe),

the reaction mechanisms and the intermediates appear to be very different, and as we will show below allows for effective metal substitution only in the acidic conditions. In the known synthesis procedures,^{28,29} a mixture of trimesic acid and NaOH typically shows high pH of about 12.^{28,29} Upon the addition of FeSO₄ solution, a dark green precipitate forms immediately and the pH drops to 7.25. The precipitate turns to orange after a few minutes due to the Fe oxidation by air (Fig. 2). Our new procedure uses a solution of sodium trimesate (see its prior synthesis in the experimental part), showing a practically neutral pH of 7.07. Upon the addition of FeSO₄ solution, it yields initially a colourless transparent solution with pH 6.08, which slowly produces a yellow precipitate turning to orange upon air oxidation (Fig. 2). The appearance and the colour of the obtained MIL-100(Fe) powders are significantly different as well as the specific surface areas and pore size distributions, despite the samples displaying the same crystal structure by PXRD (Fig. S1 and S2, ESI†).

To investigate the possibility of synthesizing mixed-metal MIL-100(Fe,M) compounds in aqueous media, we decided to first test M = cobalt. MIL-100(Fe,Co) was obtained by mixing a solution of iron and cobalt sulphates with a solution of sodium trimesate in air. This mixture allowed the reaction to proceed in an acidic media and consequently allowed the incorporation of the second metal. Synchrotron PXRD shows a single phase MIL-100(Fe,Co) (Fig. S3, ESI†) whatever the Fe/Co ratio

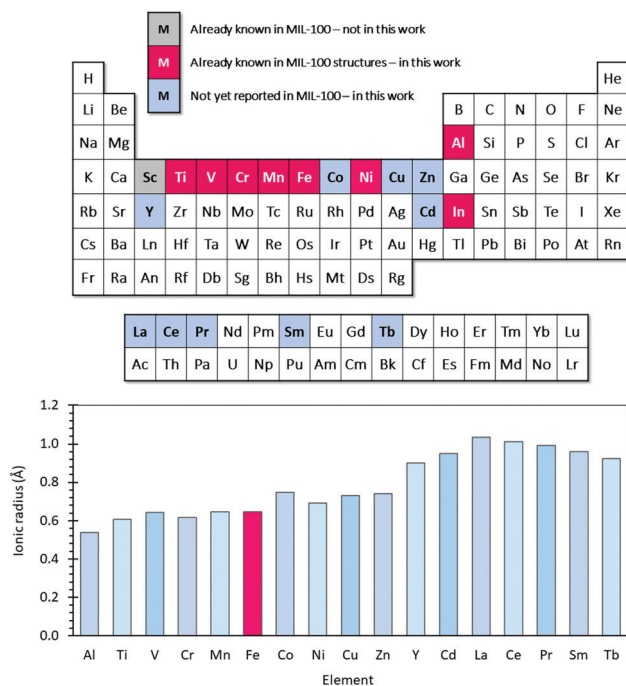


Fig. 1 Ionic radii of iron and the doping metals that were incorporated in MIL-100(Fe,M) in this work (lower part) and their position in the periodic table (upper part).

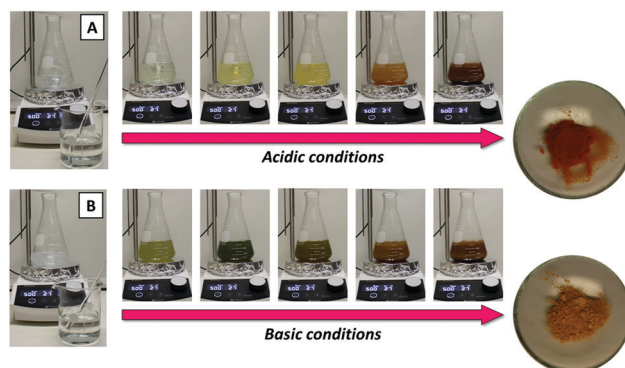


Fig. 2 Solutions before mixing (left), colour change during the reaction (middle) and the final product on a watch glass (right) for the synthesis of MIL-100(Fe) in (A) acidic and (B) basic conditions. The differences in coloration of the precipitates during the reaction indicate the existence of different reaction intermediates.

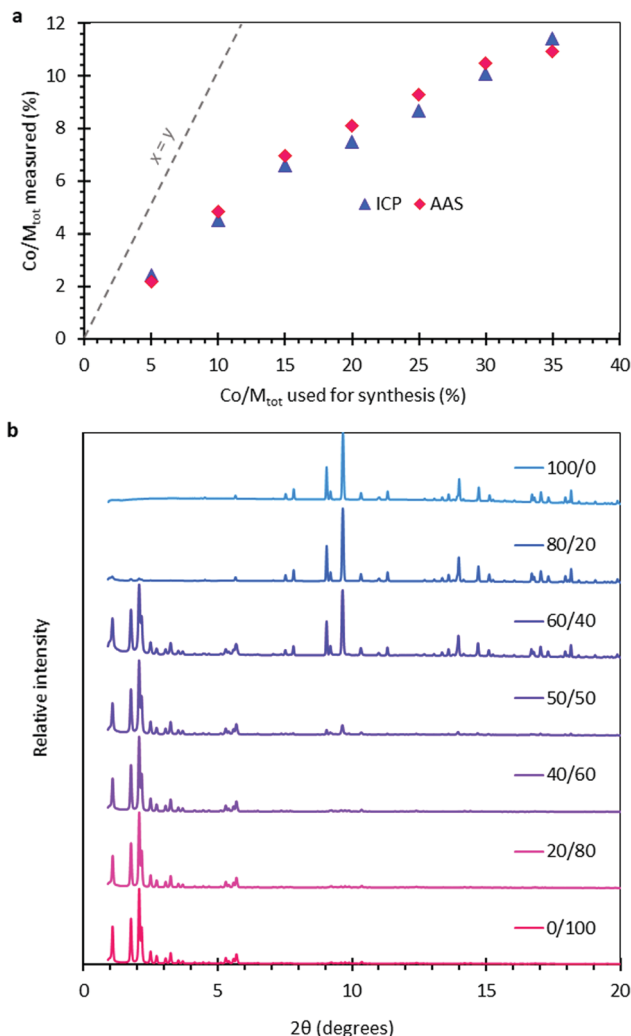
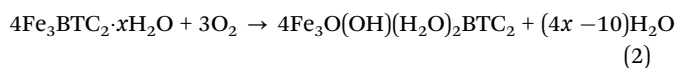
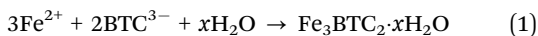


Fig. 3 (a) Incorporated quantity of cobalt into MIL-100(Fe) in function of the quantity used for the synthesis. Indicated percentages correspond to mol%. (b) PXRD patterns of compounds obtained using different Co/Fe ratios for the synthesis, showing pure MIL-100 phase for Co/Fe = 0/100 to 40/60 and the apparition of a second crystalline phase for higher Co/Fe ratios.

(in the 5–35 mol% Co range). The ATR-IR spectra are all very similar to the undoped MIL-100(Fe) (Fig. S4, ESI[†]). The incorporation of Co into the structure was confirmed and quantified by inductively coupled plasma-optical emission spectroscopy (ICP-OES) (see Fig. 3).

The formation of metal-BTC intermediates containing Fe^(II) and Co^(II) that are subsequently oxidized into MIL-100(Fe,Co) can explain why the incorporation only succeeds in acidic media, whereas in basic media it is prevented by the formation of hydroxide species. The overall reaction of the synthesis proceeds in two separate steps. At first, iron(II) trimesate precipitates, followed by oxidation in air, leading to the desired MIL-100(Fe) structure (eqn (1) and (2)).



Indeed, in the slightly acidic medium, we have successfully isolated the intermediate Fe₃BTC₂·12H₂O, as well as its Co analogue (Fig. S5, ESI[†]).

Variation of the amount of doping Co

In order to verify whether we can control the amount of incorporated doping metal, we varied the starting ratio of Fe(II) and Co(II) in the synthesis solution. The reaction time (4 h), the volume of the reaction mixture and the stirring rate were kept constant to ensure that the oxidation would proceed in the same manner. The obtained MIL-100(Fe,Co) samples were calcined and digested in aqua regia followed by ICP-OES measurements. The Co/M_{tot} ratios in the obtained MOFs were plotted against the Co/M_{tot} ratios used in the synthesis (Fig. 3a). A clear trend is observed: the amount of cobalt incorporated into the structure increases with the engaged Co/M_{tot}. However, there is a limit to the amount of Co that can be incorporated into the structure. When the used Co/M_{tot} ratio is higher than 40 mol% a second crystalline phase is present in the powder diffraction patterns (Fig. 3b). When the reaction time is increased, the amount of incorporated Co also increases. For instance, when 20 mol% of Co is used, ICP-OES shows in the resulting MIL-100(Fe,Co) a Co/M_{tot} value of 7.9 mol% after 4 h while it is 11 mol% after 24 h of reaction. For comparison purposes, we performed a post-synthetic exchange by soaking pure MIL-100(Fe) into a concentrated aqueous solution of Co²⁺. This led to a compound with very poor substitution compared to the direct synthesis, as shown by ICP (for more details see ESI[†]).

Incorporation of other doping metals

A large variety of other doping metals was used to evaluate the limits of our synthesis strategy. One would expect that at a certain size of the doping element a substitution will not occur. For this reason, we investigated the incorporation of several transition, p-block and lanthanide metals, with a particular attention on the differences in size and the possible oxidation states of the doping elements.

To our surprise, all the doping ions that can be solubilized in water substituted well into MIL-100(Fe), despite some large differences in ionic radii with Fe(III), see Fig. 1. However, a few elements are not suitable for incorporation into MIL-100(Fe) by our synthetic procedure. This is the case of Pb²⁺ that precipitates in the presence of the SO₄²⁻ ions of the iron(II) sulphate precursor, or of Bi³⁺ that undergoes oxolation in water. S-PXRD patterns (Fig. S6, ESI[†]) and ATR-IR spectra (Fig. S7, ESI[†]) of the different samples showed that they are all single phase, isostructural and that all the tested metals can be incorporated into the structure. The M_{dopant}/M_{tot} ratios obtained after 16 h reaction using 20 mol% of doping metal were determined by ICP-OES and appear to be significant (7.5 to 29.9 mol%) but dependent on the nature of the used metals (Table S1, ESI[†]). Comparison of ICP and X-ray photoelectron spectroscopy (XPS) results shows that the bulk and surface contents in a given doping metal are not always identical. This could be due to a preferential incorporation of either the doping (M) or template

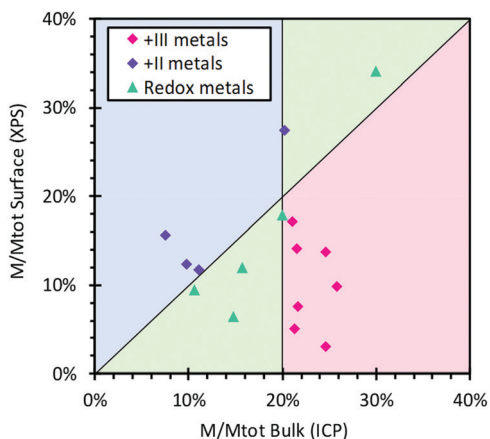


Fig. 4 Illustration of the preferential incorporation process. Metals in the +III oxidation state are incorporated preferentially over iron in MIL-100(Fe,M), leading to higher bulk than surface concentrations of M. Similarly, Fe is incorporated preferentially over +II metals. The blue and pink areas of the graph indicate the zones expected for preferential incorporation of Fe over M and of M over Fe respectively. The doping metals undergoing redox during the formation of the MOF are all located in the green areas, indicating the existence of more complex processes during the incorporation of those metals. The M/Fe ratio used for all syntheses was 20/80. Indicated percentages correspond to mol%.

metal (Fe) and the subsequent variation of the relative concentrations of the metals in solution during the crystal growth.^{42–44} Metals that are preferentially incorporated are then more concentrated in the core of the crystal than on its surface. This theory is supported for the +II and +III doping metals that do not undergo oxidation neither reduction during the incorporation process. Indeed, the iron, being oxidized from +II to +III during the formation of the MOF, is incorporated preferentially over +II metals (Co^{2+} , Ni^{2+} , Zn^{2+} and Cd^{2+}) but not over +III metals (Al^{3+} , Cr^{3+} , Y^{3+} and Ln^{3+}). However, when the doping metal undergoes redox during the incorporation (*i.e.* Cu, Ti, V), more complex processes are at work, as shown in Fig. 4. The clear-cut regions of the preferential substitution with respect to the oxidation states of the doping metal, illustrated in Fig. 4, suggest satisfactory rationalization of the obtained results and potentially a predictive power for the incorporation of other metals.

Materials porosities

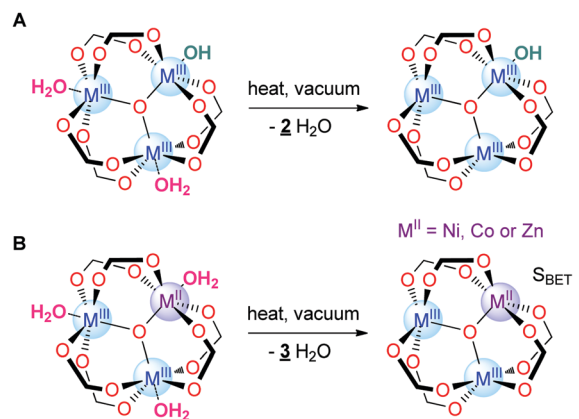
Before nitrogen sorption experiments, all materials were activated by heating under vacuum at 200 °C for 10 hours. Importantly, all the obtained materials sustained this activation step without collapsing of the structures. The BET surface areas of the MIL-100(Fe,M) materials were very high for most doping metals (Fig. S8, ESI†). Nearly all the obtained compounds show nitrogen absorption–desorption curves with a very similar shape; of the I(a) type according to the IUPAC classification of physisorption isotherms,⁴⁵ characteristic of purely microporous materials (Fig. S8, ESI†). However, for M = Cr the surface area is significantly lower than with other first-row transition metals. Second-row transition metals show smaller, although still large, surface areas ($S_{\text{BET}} = 1350 \text{ m}^2 \text{ g}^{-1}$ for M = Y and $1462 \text{ m}^2 \text{ g}^{-1}$ for M = Cd).

The rare-earth elements, Sm and Tb, also show similar surface areas. However, La and especially Pr and Ce show reduced surface areas; going below $1000 \text{ m}^2 \text{ g}^{-1}$. Those samples contain secondary phases revealed by PXRD. These phases disappear at high temperatures and reappear only after rehydration (Fig. S9D, ESI†). Noticeably, the temperature at which those secondary phases disappear is dependent on the ionic radius of the lanthanide metal (the larger the doping metal, the higher the temperature needed for eliminating the secondary phase) (Fig. S9A and B, ESI†). XPS measurements on those samples show that some sodium is present on the surface (Fig. S10, ESI†). The reduced surface areas can thus be explained by the presence of sodium salts, undergoing crystal to amorphous dehydration. A similar secondary phase is present in MIL-100(Fe,Y) (Fig. S9C, ESI†). More importantly, MIL-100(Fe,M) with doping metals having typical oxidation state +II, namely Ni, Co and Zn, show about 10% higher surface areas than MIL-100(Fe) likely due to the improved dehydration of the metal sites, see Scheme 1. The surface area of the nickel-doped MOF ($2274 \text{ m}^2 \text{ g}^{-1}$) is significantly larger than the one of MIL-100(Fe,Ni) materials previously reported ($1525\text{--}1570 \text{ m}^2 \text{ g}^{-1}$).⁴¹

Interestingly, the MIL-100(Fe,M) samples with M = Cu, Al, V and Ti show a slight hysteresis in their sorption–desorption curves. S-PXRD patterns of those three compounds also show peak broadening as compared to the other materials. These observations suggest the presence of mesopores and/or inter-grain porosities into the materials.

Thermal behaviour

The thermal stability of the obtained compounds was evaluated by TGA measurements under both nitrogen and air. All the compounds, with the notable exception of MIL-100(Fe,Cu) show very similar decomposition temperatures under nitrogen (around 420 °C), as well as under air (around 355 °C) (Fig. S11, ESI† and Fig. 5). The presence of copper in MIL-100(Fe,Cu) has an important impact on the thermal stability of the compound as the decomposition temperature drops from ~ 355 °C to 327 °C under air and from ~ 420 °C to 354 °C under nitrogen.



Scheme 1 (A) Only two water molecules can be desorbed from $\text{Fe}_2\text{M}^{\text{III}}\text{-}\mu_3\text{-oxo}$ clusters whereas (B) three water molecules can be desorbed from $\text{Fe}_2\text{M}^{\text{II}}\text{-}\mu_3\text{-oxo}$ clusters, leading to higher surface areas.

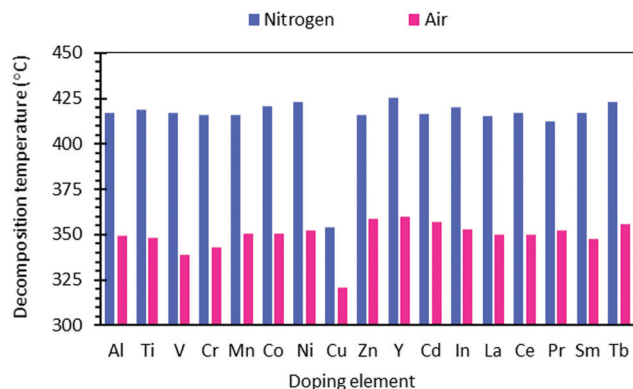


Fig. 5 Decomposition temperatures of the MIL-100(Fe,M) compounds determined by TGA under air and nitrogen.

Heating the samples at a rate of 10 K min^{-1} did not allow to get rid of all the coordinated solvent molecules before the decomposition, even if this last event occurs at temperatures above $400 \text{ }^\circ\text{C}$ ($354 \text{ }^\circ\text{C}$ in the case of MIL-100(Fe-Cu)). This can be explained by the strong bonds formed between the coordinated solvent molecules and the metal centres.

Determination of oxidation states

XPS was used to determine the oxidation states of the incorporated doping metals. The analysis revealed that oxidation states depend highly on the nature of the doping metal, ranging from +I to +V (Fig. S12, ESI†). The incorporation of metals with the oxidation states +II, +III and +IV can easily be accommodated by varying the nature of the oxygenated ligand on the doping metal site (Fig. 6, upper part). If we consider that only one doping metal atom is present in each $\text{M}_3\text{-}\mu_3\text{-oxo}$ cluster (*i.e.* $\text{Fe}_2\text{M-}\mu_3\text{-oxo}$ clusters) at the maximum, and that the iron centres are in the +III oxidation state, then M(II) does not need any counter ion. Similarly, M(III) is balanced by OH^-

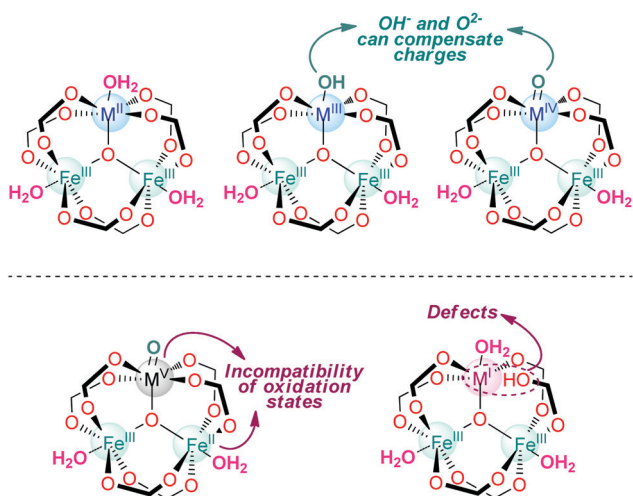


Fig. 6 Illustration of neutral $\text{Fe}_2\text{M-}\mu_3\text{-oxo}$ clusters that can be formed with M in oxidation states +II, +III and +IV with charge balance by OH^- or O^{2-} units (upper part) and problems arising in the charge balance in the presence of doping metals in the +I or +V oxidation states.

(the presence of Cl^- or SO_4^{2-} was not detected by XPS) and M(IV) is balanced by $\mu_1\text{-O}^{2-}$ ions.

On the other hand, the presence of Cu(I), that is detected in MIL-100(Fe,Cu), cannot be explained by a perfect cluster structure. It is likely that in this case defects are present in significant amounts in the cluster or in the framework structure (Fig. 6, lower part). This nicely correlates with the hysteresis observed on the nitrogen sorption isotherm, peak broadening in the diffraction patterns, as well as the lower thermal stability of MIL-100(Fe,Cu). For MIL-100(Fe,V), V^{5+} was detected along with V(IV) and V(III). The +V oxidation state of the doping metal is also incompatible with a perfect cluster structure (unless one of the iron atoms is present in the +II oxidation state, but this is again incompatible with the strong oxidation potential of V^{5+}), see Fig. 6, lower part. Defects around the V^{5+} centres must therefore be considered in this case too, correlated again with the hysteresis observed on the nitrogen sorption isotherm of MIL-100(Fe,V) and peak broadening in the diffraction profiles.

Using PXRD for doping metal quantification

Finally, a methodological development made in the course of this work deserves a discussion. The most usual methods for dosing the metals in MOFs, and more specifically bimetallic MOFs, include ICP and Atomic Absorption Spectroscopy (AAS). However, these methods need digestion of the sample and a dilution prior to analysis. Also, a standard curve must be established for both methods. Moreover, a different hollow cathode lamp must be used for quantifying each different metal by AAS. For this reason, it would be convenient to have a valid method for simultaneously determining the metal content and the $M_{\text{dopant}}/M_{\text{tot}}$ ratio without need for sample digestion and dilution. PXRD would be a convenient way to determine this by Rietveld refinement as most laboratories working on MOFs have access to this method. However, the complex structure of MIL-100(Fe,M) compounds and the difficulty to attain complete removal of solvents and guests from the pores does not allow to accomplish metal content determination using this method directly on the MIL-100 compounds. However, we tested a strategy that consists in calcination of the sample in air followed by measuring the PXRD pattern of the resulting oxides (Fig. S13, ESI†) and subsequent Rietveld refinement, allowing to determine $M_{\text{dopant}}/M_{\text{tot}}$. Here we show that this determination is quite precise in the specific cases where two oxides having different crystal structures are obtained. For example, calcination of MIL-100(Fe,Co) leads to a mixture of Fe_2O_3 and CoFe_2O_4 . Once Rietveld refinement is performed and the weight fractions of Fe_2O_3 and CoFe_2O_4 are determined, the metal ratio can easily be calculated (see ESI†). This method does not apply in case solid solutions form or isostructural oxides with similar cell dimensions are obtained. For example, MIL-100(Fe,Cr) is oxidized into $(\text{Fe,Cr})_2\text{O}_3$, Rietveld refinement is thus of no use for metal quantification. When the main and the doping metals have a large difference in number of electrons (*i.e.* Al and Fe) or when absorption coefficients are too high, the method also gives uncertain results

(although absorption correction in Rietveld refinement can be applied to a certain extent). The main advantage of this method is that the analysis can be coupled to TGA measurements, by measuring a PXRD pattern of the combustion residue. Characterization by TGA and by ICP (or AAS) measurements *via* conventional methods would require the destruction of a larger amount of sample than the method we propose. The precision of our method was tested against ICP and AAS for MIL-100(Fe,Co) and against ICP for MIL-100(Fe,M) (M = Cr, Co, Ni, Cu and Zn), showing its validity (see Fig. S13, ESI†).

Experimental

Materials and methods

Synchrotron Powder X-ray diffraction (S-PXRD) patterns of MIL-100(Fe,M) samples were recorded at the Swiss-Norwegian beamlines (SNBL) at the European Synchrotron Radiation Facility (ESRF, Grenoble, France) at a wavelength of 0.68683 Å or 0.79800 Å using a Pilatus 2M detector. The samples were loaded into glass capillaries of 0.5 mm diameter. For temperature dependent measurements, a calibrated heating gas blower was used and the samples were heated from room temperature to 500 °C.

ATR-IR spectra were recorded using a Bruker Alpha spectrometer equipped with a Platinum ATR module (diamond crystal) housed in an MBraun argon-filled glovebox. Spectra were recorded in the range of 4000–370 cm⁻¹ with a resolution of 4 cm⁻¹.

Nitrogen sorption measurements at 77 K were performed on a Micromeritics ASAP 2020 instrument. All samples were degassed at 200 °C during 10 h prior to analysis.

XPS analyses were carried out with a SSI-X-probe (SSX 100/206) photoelectron spectrometer from Surface Science Instruments, equipped with a monochromatized microfocus Al X-ray source. The samples were prepared by sticking on a double-face adhesive tape mounted onto small brass samples holders that were placed on an insulating ceramic carousel (Macor). An electron flood gun combined with a nickel grid were used to avoid charge effects. The CasaXPS software (Casa Software Ltd) was used to perform the data treatment.

ICP-AES measurements were performed after sample calcination at 500 °C followed by digestion in aqua regia. An ICAP-6500 apparatus from ThermoFisher Scientific was used to carry out the analyses.

For AAS, samples were digested in aqua regia followed by filtration to remove the reprotonated H₃BTC. AAS measurements were performed using a PerkinElmer 3110 atomic absorption spectrometer. For Fe and Co analysis, an oxidizing air-acetylene flame was used to atomize the samples. Intensitron™ hollow cathode lamps (PerkinElmer) were used for the measurements (pure Co cathode for cobalt determination and mixed FeNiCu lamp for Fe determination).

Lab PXRD analyses of calcined MIL-100(Fe,M) samples were performed using a MAR345 diffractometer with X-rays

generated by a Rigaku UltraX 18S X-ray generator (molybdenum anode, 0.71073 Å), with a monochromated beam (Xenocs FOX 3D mirror).

TGA/DSC measurements under air and nitrogen were recorded on a Mettler Toledo TGA/DSC 3+ STAR^e System. Gas flows of 100 ml min⁻¹ and heating rates of 10 °C min⁻¹ were used.

NMR spectra were recorded at room temperature (296 K) on a Bruker Avance II 300 spectrometer operating at 300.1 MHz for ¹H and 75.76 MHz for ¹³C. Experiments were run under TopSpin program (3.2 version, Bruker) using a BBO or a BBFO {¹H,X} probeheads equipped with a z-gradient coil.

Chemicals

Trimesic acid (98%) and sulphuric acid (96%) were purchased from Acros Organics. Denaturated ethanol (Technisolv, 99%), diethyl ether (GPR Rectapur), hydrochloric acid (37%) and sodium hydroxide pellets were purchased from VWR Chemicals. Iron sulphate (technical grade) was supplied from Forever products. Cobalt(II) sulphate heptahydrate (99+%) was purchased from Janssen Chimica. Copper(II) chloride dihydrate was purchased from Riedel-deHaën. Cadmium nitrate hexahydrate (99.9%), aluminium chloride (99.9%), vanadium(III) chloride (97%) and titanium(III) chloride (99.999%) were purchased from Sigma-Aldrich. Cobalt(II) chloride hexahydrate (98%) was purchased from Fluka. Nickel(II) chloride hexahydrate, yttrium(III) nitrate pentahydrate and potassium dichromate (99.8%) were purchased from Merck. Praseodymium(III,IV) oxide (99.9%) was purchased from Acros. Lanthanum(III) carbonate was purchased from K&K Laboratories, Inc. Samarium(III) oxide (99.9%) was purchased from Koch-Light Laboratories Ltd. Manganese(II) chloride (98%), cerium(III) acetate hydrate (99.9%) and terbium(III) nitrate hexahydrate (99.999%) was purchased from Aldrich. Zinc chloride (98%) was purchased from Alfa Aesar.

All chemicals were used as received except for iron sulphate, which was purified by heating a saturated solution in boiling water in the presence of iron metal and sulphuric acid for one hour. The obtained hot solution was filtered and allowed to cool. Ethanol was added to the solution to crystallize the iron sulphate, which was isolated by filtration on a glass frit. The purified FeSO₄ heptahydrate was washed with ethanol and dried under vacuum (using a Schlenk line).

Synthesis of MIL-100(Fe) in basic conditions (old procedure)

H₃BTC (1.42 g) and NaOH (0.80 g) were added to 125 ml of deionized water and the solution was sonicated until all the H₃BTC was dissolved (pH = 12). A second solution was made by dissolving 2.25 g of FeSO₄·7H₂O in 125 ml of water (pH = 4.87). Both solutions were mixed and allowed to react in the presence of air (in a 500 ml erlenmeyer flask, 500 rpm agitation) for 15 hours. Immediately after addition, the measured pH was 7.25, and the obtained precipitate dark green, then the colour turned to orange upon oxidation. The precipitate was separated from the supernatant liquid by centrifugation and washed using 3 × 50 ml of deionized water and 3 × 50 ml of denaturated ethanol.

The obtained solid was then dried using a rotary evaporator at 70 °C and once the powder was dry, the evaporation flask was allowed to cool under vacuum, using a Schlenk line.

Synthesis of MIL-100(Fe) in acidic conditions (new procedure)

Na₃BTC trihydrate was obtained by adding 1 eq. of H₃BTC to 3 eq. NaOH in a minimum amount of water. The obtained solution was filtered to remove any unreacted trimesic acid. Ethanol was added to the filtrate to precipitate the sodium trimesate. The obtained compound was filtered and washed with ethanol to remove any unreacted NaOH (the pH was tested using a paper indicator) and then with diethylether. The obtained white fluffy very light powder was then dried in a large beaker in an oven at 45 °C overnight. ¹H NMR (300.1 MHz, D₂O) δ 8.42 (s, 3H). ¹³C NMR (75.76 MHz, D₂O) δ 174.75, 136.53, 131.43. TGA weight loss upon dehydration: exp. 17.8%, calc. 16.4%.

1.86 g of Na₃BTC trihydrate was dissolved in 125 ml of deionized water. A second solution was made by dissolving 2.25 g of FeSO₄·7H₂O in 125 ml of water (pH = 4.87). Both solutions were mixed together and allowed to react in the presence of air (in a 500 ml erlenmeyer flask, 500 rpm agitation) for 15 hours. Immediately after addition, the measured pH was 6.08, and a yellow precipitate appeared slowly, then the colour turned to orange upon oxidation. The precipitate was separated from the supernatant liquid by centrifugation and washed using 3 × 50 ml of deionized water and 3 × 50 ml of denaturated ethanol. The obtained solid was then dried using a rotary evaporator at 70 °C and once the powder was dry, the evaporation flask was allowed to cool under vacuum, using a Schlenk line.

Synthesis of CrCl₃ hexahydrate

Chromium(III) chloride was synthesized by gently adding 5.92 g of K₂Cr₂O₇ with 20 ml of methanol in 17 ml of concentrated HCl (37%). This reaction was carried out in a very large erlenmeyer flask placed in an ice bath (the reaction is very exothermic). The obtained solution was then boiled to dryness and the obtained green solid was washed with ethanol and ether followed by drying under vacuum. FTIR 3526 cm⁻¹ (sharp), 2986 cm⁻¹ (broad), 1584 cm⁻¹, 888 cm⁻¹, 722 cm⁻¹, 612 cm⁻¹, 494 cm⁻¹, 408 cm⁻¹, the spectrum corresponds to reference data.⁴⁶

Synthesis of LaCl₃, SmCl₃ and PrCl₃ hydrates

To 3 eq. of concentrated (37%) aqueous HCl was added 1 eq. Ln in the form of the corresponding oxide (La₂O₃, Sm₂O₃ or Pr₆O₁₁). The oxide was reacted with the acid until a clear solution was obtained. Then excess acetone was added to remove the excess water and the organic and aqueous layers were shaken vigorously. The organic layer was then eliminated by decantation. This operation was repeated until a solid started to precipitate in the aqueous layer. The solid was then filtered using a glass frit and acetone was used to wash the resulting crystals. The salt was then dried under vacuum (using a Schlenk line) and stored in a desiccator. FTIR LaCl₃·xH₂O: 3356 cm⁻¹ (broad), 2117 cm⁻¹, 1616 cm⁻¹ (sharp, intense),

582 cm⁻¹, 415 cm⁻¹; SmCl₃·xH₂O: 3330 cm⁻¹, 3226 cm⁻¹ (broad), 2235 cm⁻¹, 1624 cm⁻¹ (sharp, intense), 1084 cm⁻¹ (broad), 586 cm⁻¹, 448 cm⁻¹; PrCl₃·xH₂O 3330 cm⁻¹, 3222 cm⁻¹ (broad), 2226 cm⁻¹, 1628 cm⁻¹ (sharp, intense), 1080 cm⁻¹ (broad), 574 cm⁻¹, 440 cm⁻¹.

Synthesis of MIL-100(Fe,M) in acidic conditions (new procedure)

The syntheses of the doped MIL-100(Fe,M) MOFs were realized by following the identical procedure to that for the synthesis of MIL-100(Fe) in acidic conditions. The only difference is that the 2.25 g of iron sulphate were replaced by a mixture of FeSO₄·7H₂O and another metal salt in different ratios. Table S2A (ESI[†]) lists the used salts and their respective quantities. The pH and the colours of the different precipitates is also given in Table S2B (ESI[†]).

Conclusions

We developed a green method for synthesizing bimetallic MIL-100(Fe,M) compounds at room-temperature in water, avoiding energy demanding solvothermal processes and avoiding the use of strong mineral acids, all these conditions are good prerequisites for an easy scale up. This synthesis is performed in a single step, and therefore is less time-consuming and more efficient than post-synthetic exchange approaches. We showed that the incorporation of doping metals is only possible at pH values below 7 and that Na₃BTC·3H₂O is a useful ligand source. Importantly, we demonstrated that the amount of the incorporated doping metal can be tuned in a controlled manner. Metals in the +II as well as +V oxidation states and lanthanides were incorporated as dopants into the structure of MIL-100(Fe) for the first time. We showed that large differences between the ionic radius of the doping and the templating metals does not lead to phase segregation. We also showed that the incorporation of Cu(I) drastically lowers the thermal stability of MIL-100(Fe,Cu) and that the incorporation of V, Al and Ti induces formation of mesopores. Finally, we developed a PXRD-based method that can be combined with TGA to easily access the metal ratios in complex mixed-metal MOFs with less sample required than for the currently used ICP and AAS based methods.

The obtained MIL-100(Fe,M) compounds could serve in fields like gas sorption and catalysis. On the one hand, the presence of metals in the +II oxidation state can strongly influence the absorption of CO₂ or could serve in redox catalysis. On the other hand, the presence of lanthanide and other high oxidation state metals could serve as efficient Lewis acid sites for catalysis. Research in these directions is currently underway in our laboratory.

Conflicts of interest

There are no conflicts to declare.

Acknowledgements

The authors acknowledge financial support through the FRIA funding of F.R.S./FNRS for T. S. and the FNRS for grants EQP U.N038.13 and CdR J.0164.17. Dr Dmitry Chernyshov and Dr Iurii Dovgaliuk are acknowledged for their help during synchrotron measurements at the SNBL of the ESRF in Grenoble. We thank Dr Pierre Eloy for help with the XPS measurements and interpretation of the data, Dr Koen Robeyns for his help with PXRD measurements, Anne Iserentant for the ICP measurements and Jean-François Statsyns for his help with the AAS and TGA measurements.

Notes and references

- 1 H. Li, K. Wang, Y. Sun, C. T. Lollar, J. Li and H. Zhou, *Mater. Today*, 2018, **21**, 108–121.
- 2 Y. Zhu, Y. Wang, S. Zhao, P. Liu, C. Wei, Y. Wu, C. Xia and J. Xie, *Inorg. Chem.*, 2014, **53**, 7692–7699.
- 3 H. Le, Q. Hui, D. Zhang, G. Ye, W. Zhou, C. Hou, W. Xu and Y. Sun, *New J. Chem.*, 2017, **41**, 13504–13509.
- 4 A. Corma, H. García and F. X. Llabres i Xamena, *Chem. Rev.*, 2010, **110**, 4606–4655.
- 5 *Zeolites and Zeolite-like Materials*, ed. B. F. Sels and L. M. Kustov, Elsevier, 2016.
- 6 X. Zhao, Y. Wang, D. Li, X. Bu and P. Feng, *Adv. Mater.*, 2018, **30**, 1705189.
- 7 S. Homayoonnia and S. Zeinali, *Sens. Actuators, B*, 2016, **237**, 776–786.
- 8 R. Li, X. Ren, H. Ma, X. Feng, Z. Lin, X. Li, C. Hu and B. Wang, *J. Mater. Chem. A*, 2014, **2**, 5724–5729.
- 9 F. Jeremias, A. Khutia, S. K. Henninger and C. Janiak, *J. Mater. Chem.*, 2012, **22**, 10148–10151.
- 10 J. B. DeCoste, G. W. Peterson, B. J. Schindler, K. L. Killops, M. A. Broweb and J. J. Mahle, *J. Mater. Chem. A*, 2013, **1**, 11922–11932.
- 11 K. Müller, N. Vankova, L. Schöttner, T. Heine and L. Heinke, *Chem. Sci.*, 2019, **10**, 153–160.
- 12 J. Wang, Y. Zhang, M. Li, S. Yan, D. Li and X. Zhang, *Angew. Chem., Int. Ed.*, 2017, **56**, 6478–6482.
- 13 S. Yuan, J. Qin, C. T. Lollar and H. Zhou, *ACS Cent. Sci.*, 2018, **4**, 440–450.
- 14 S. Yuan, L. Feng, K. Wang, J. Pang, M. Bosch, C. Lollar, Y. Sun, J. Qin, X. Yang, P. Zhang, Q. Wang, L. Zou, Y. Zhang, L. Zhang, Y. Fang, J. Li and H. C. Zhou, *Adv. Mater.*, 2018, **30**, 1704303.
- 15 F. Jeremias, S. K. Henninger and C. Janiak, *Dalton Trans.*, 2016, **45**, 8637–8644.
- 16 S. Cui, M. Qin, A. Marandi, V. Steggles, S. Wang, X. Feng, F. Nouar and C. Serre, *Sci. Rep.*, 2018, **8**, 15284.
- 17 S. Wang and C. Serre, *ACS Sustainable Chem. Eng.*, 2019, **7**, 11911–11927.
- 18 Y. Sun and H. Zhou, *Sci. Technol. Adv. Mater.*, 2015, **16**, 054202.
- 19 S. Huang, K. Yang, X. Liu, H. Pan, H. Zhang and S. Yang, *RSC Adv.*, 2017, **7**, 5621–5627.
- 20 Y.-R. Chen, K.-H. Liou, D.-Y. Kang, J.-J. Chen and L.-C. Lin, *Langmuir*, 2018, **34**, 4180–4187.
- 21 D. Kim, H. Kim and D. Cho, *Catal. Commun.*, 2016, **73**, 69–73.
- 22 Y. Shi, C. Li, X. Liu, H. Zhang, Q. Zhao and X. Li, *Integr. Ferroelectr.*, 2017, **181**, 14–25.
- 23 P. L. Llewellyn, S. Bourrelly, C. Serre, A. Vimont, M. Daturi, L. Hamon, G. De Weireld, J.-S. Chang, D. Hong, Y. K. Hwang, S. H. Jhung and G. Férey, *Langmuir*, 2008, **24**, 7245–7250.
- 24 C. K. Brozek and M. Dinca, *J. Am. Chem. Soc.*, 2013, **135**, 12886–12891.
- 25 S. Abednatanzi, P. G. Derakhshandeh, H. Depauw, F.-X. Coudert, H. Vrielinck, P. Van Der Voort and K. Leus, *Chem. Soc. Rev.*, 2019, **48**, 2535–2565.
- 26 S. Wongsakulphasatch, F. Nouar, J. Rodriguez, L. Scott, C. Le Guillouzer, T. Devic, P. Horcajada, P. L. Llewellyn, A. Vimont, G. Clet, M. Daturi and C. Serre, *Chem. Commun.*, 2015, **51**, 10194–10197.
- 27 A. Dhakshinamoorthy, A. M. Asiric and H. Garcia, *Catal. Sci. Technol.*, 2016, **6**, 5238–5261.
- 28 K. Guesh, C. Caiuby, Á. Mayoral, M. Díaz-García, I. Díaz and M. Sanchez-Sanchez, *Cryst. Growth Des.*, 2017, **17**, 1806–1813.
- 29 H. Tian, J. Peng, Q. Du, X. Hui and H. He, *Dalton Trans.*, 2018, **47**, 3417–3424.
- 30 M. Sánchez-sánchez, N. Getachew, M. Díaz-garcía, Y. Chebude and I. Díaz, *Green Chem.*, 2015, **17**, 1500–1509.
- 31 V. F. Cheong and P. Y. Moh, *Mater. Sci. Technol.*, 2018, **34**, 1025–1045.
- 32 R. D. Shannon, *Acta Crystallogr., Sect. A: Cryst. Phys., Diffraction, Theor. Gen. Crystallogr.*, 1976, **32**, 751–767.
- 33 C. P. Cabello, P. Rumori and G. T. Palomino, *Microporous Mesoporous Mater.*, 2014, **190**, 234–239.
- 34 L. Mitchell, P. Williamson, B. Ehrlichová, A. E. Anderson, V. R. Seymour, S. E. Ashbrook, N. Acerbi, L. M. Daniels, R. I. Walton, M. L. Clarke and P. A. Wright, *Chem. – Eur. J.*, 2014, **100**, 17185–17197.
- 35 C. P. Cabello, G. Gómez-pozuelo and M. Opanasenko, *Chem-PlusChem*, 2016, **81**, 828–835.
- 36 M. N. Timofeeva, V. N. Panchenko, N. A. Khan, Z. Hasan, I. P. Prosvirin, S. V. Tsybulya and S. H. Jhung, *Appl. Catal., A*, 2017, **529**, 167–174.
- 37 G. Gema, P. Cabello and M. Opanasenko, *ChemPlusChem*, 2017, **82**, 152–159.
- 38 W. Zhang, Y. Shi, C. Li, Q. Zhao and X. Li, *Catal. Lett.*, 2016, **146**, 1956–1964.
- 39 L. Zou, D. Feng, T.-F. Liu, Y.-P. Chen, S. Yuan, K. Wang, X. Wang, S. Fordhama and H.-C. Zhou, *Chem. Sci.*, 2016, **7**, 1063–1069.
- 40 J. Castells-gil, N. M. Padiál, N. Almora-Barrios, I. Da Silva, D. Mateo, J. Albero, H. García and C. Martí-Gastaldo, *Chem. Sci.*, 2019, **10**, 4313–4321.
- 41 M. Giménez-Marqués, A. Santiago-Portillo, S. Navalón, M. Álvaro, V. Briois, F. Nouar, H. Garcia and C. Serre, *J. Mater. Chem. A*, 2019, **7**, 20285–20292.

- 42 H. Depauw, I. Nevjestic, J. De Winne, G. Wang, A. Verberckmoes, C. Detavernier, F. Callens, E. De Canck, H. Vrielinck and P. Van Der Voort, *Chem. Commun.*, 2017, **53**, 8478–8481.
- 43 Y. Jiao, C. R. Morelock, N. C. Burtch, W. P. Moun, J. T. Hungerford and K. S. Walton, *Ind. Eng. Chem. Res.*, 2015, **54**, 12408–12414.
- 44 L. J. Wang, H. Deng, H. Furukawa, F. Ga, K. E. Cordova, D. Peri and O. M. Yaghi, *Inorg. Chem.*, 2014, **53**, 5881–5883.
- 45 M. Thommes, K. Kaneko, A. V. Neimark, J. P. Olivier, F. Rodriguez-reinoso, J. Rouquerol and K. S. W. Sing, *Pure Appl. Chem.*, 2015, **87**, 1052–1069.
- 46 V. Stefov and V. M. Petrus, *J. Mol. Struct.*, 1999, **482–483**, 109–113.